

Ferroelectric atomic displacement in multiferroic tetragonal perovskite $\text{Sr}_{1/2}\text{Ba}_{1/2}\text{MnO}_3$

D. Okuyama,^{1,*} K. Yamauchi,² H. Sakai,^{3,4} Y. Taguchi,⁵ Y. Tokura,^{5,6} K. Sugimoto,⁷ T. J. Sato,¹ and T. Oguchi²

¹*Institute of Multidisciplinary Research for Advanced Materials (IMRAM), Tohoku University, Katahira 2-1-1, Sendai 980-8577, Japan.*

²*ISIR-SANKEN, Osaka University, 8-1 Mihogaoka, Ibaraki, Osaka 567-0047, Japan*

³*Department of Physics, Osaka University, Toyonaka, Osaka 560-0043, Japan*

⁴*PRESTO, Japan Science and Technology Agency, Kawaguchi, Saitama 332-0012, Japan*

⁵*RIKEN Center for Emergent Matter Science (CEMS), Wako 351-0198, Japan*

⁶*Department of Applied Physics, University of Tokyo, Tokyo 113-8656, Japan*

⁷*JASRI SPring-8, Hyogo 679-5198, Japan*

(Dated: February 18, 2022)

We investigate the crystal structure in multiferroic tetragonal perovskite $\text{Sr}_{1/2}\text{Ba}_{1/2}\text{MnO}_3$ with high accuracy of the order of 10^{-3} Å for an atomic displacement. The large atomic displacement for Mn ion from the centrosymmetric position, comparable with the off-centering distortion in the tetragonal ferroelectric BaTiO_3 , is observed in the ferroelectric phase ($T_N \leq T \leq T_C$). In stark contrast, in the multiferroic phase ($T \leq T_N$), the atomic displacement for Mn ion is suppressed, but those for O ions are enlarged. The atomic displacements in the polar crystal structures are also analyzed in terms of the ferroelectric modes. In the ferroelectric phase, the atomic displacements are decomposed into dominant positive Slater, negative Last, and small positive Axe modes. The suppression of Slater and Last modes, the sign change of Last mode, and the enlargement of Axe mode are found in the multiferroic phase. The ferroelectric distortion is well reproduced by a first-principles calculation based on Berry phase method, providing an additional information on competing mechanisms to induce the polarization, electronic p - d hybridization vs. magnetic exchange-striction.

I. INTRODUCTION

Since a large nonlinear magnetoelectric effect was found in perovskite TbMnO_3 , multiferroic materials have been extensively investigated¹⁻⁴. It is well known that the electric polarization of the most multiferroic materials is far smaller than those of conventional ferroelectric materials such as BaTiO_3 . Nevertheless, rather large electric polarization among the multiferroic materials are theoretically shown in tetragonal perovskite BaMnO_3 ⁵⁻⁷. In the paramagnetic phase, it is prospected that the ferroelectricity is induced by the off-centering distortion of the Mn and O ions. Since the magnetic Mn^{4+} ion directly contributes to the emergence of the ferroelectricity, the large magnetoelectric effect is expected. However, in fact, it was known that the hexagonal structural phase is stable in BaMnO_3 . Sakai *et al.* found that $\text{Sr}_{1/2}\text{Ba}_{1/2}\text{MnO}_3$ with the smaller tolerance factor is crystallized in the tetragonal perovskite structure and shows ferroelectricity⁸. Below the magnetic phase transition temperature, the change of the crystal lattice with large reduction of the electric polarization is observed in tetragonal perovskite $\text{Sr}_{1/2}\text{Ba}_{1/2}\text{MnO}_3$ ⁸.

Perovskite $\text{Sr}_{1/2}\text{Ba}_{1/2}\text{MnO}_3$ exhibits two phase transitions, ferroelectric and antiferromagnetic, at $T_C \sim 400$ K and $T_N \sim 185$ K⁸, respectively. Here, we call the phases for $T_N \leq T \leq T_C$ as ferroelectric and for $T \leq T_N$ as multiferroic, respectively. Below T_C , it is reported that the crystal system changes from the centrosymmetric cubic to the polar tetragonal, determined from the temperature variation of the c/a -lattice-constant ratio. The c/a increases with decreasing temperature below T_C and sat-

urates near 250 K. In contrast, below T_N , the c/a turns to decrease with decreasing temperature and saturates below 150 K. From the reduction of c/a , it was speculated that the electric polarization is also reduced. The crystal structure analyses with use of the twin-free single crystal was also performed in the ferroelectric phase⁸. The result indicates that the origin of the ferroelectricity is the off-centering distortion of O1-Mn-O1 bond angle, same with the tetragonal ferroelectric BaTiO_3 [See Fig. 1 (a)]⁹⁻¹¹. In the multiferroic phase, the distortion of O1-Mn-O1 at 50 K is smaller than that at 225 K in the ferroelectric phase. In view of the phase continuity from the antiferromagnetic ordered phase of SrMnO_3 ^{12,13}, the antiferromagnetic structure in the multiferroic phase is inferred to be G-type (G-AFM), in which nearest neighbor magnetic moments are aligned antiparallel as shown in Fig. 1 (b). In the earlier study, it was speculated that the ferroelectric polarization is suppressed to obtain the gain of the magnetic exchange energy^{8,14}. To our best knowledge, however, the quantitative comparison between the experimental result and the theoretical calculation for the electric polarization in the multiferroic phase has not yet been done. To quantitatively discuss the suppression mechanism of the ferroelectric polarization, information of the atomic displacements and the frozen ferroelectric modes in the ferroelectric and multiferroic phases is necessary. Nonetheless, in the earlier crystal structure analysis, the obtained atomic displacements of the ions in multiferroic phase is smaller than the experimental uncertainties⁸. Thus, the accurate crystal structure analysis in the multiferroic phase of tetragonal perovskite $\text{Sr}_{1/2}\text{Ba}_{1/2}\text{MnO}_3$ has been desired.

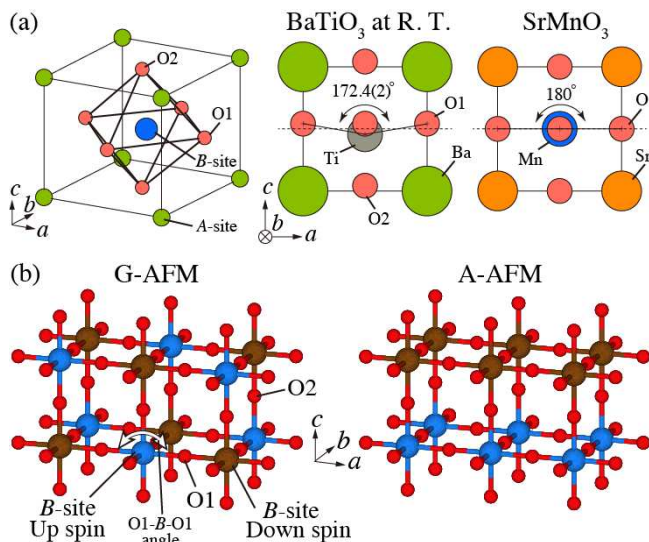


FIG. 1: (Color online) (a) Schematic illustrations of the perovskite ABO_3 structure. The O1-B-O1 bond angles of the $BaTiO_3$ and $SrMnO_3$ are also shown. (b) Schematics to explain the G-type antiferromagnetic (G-AFM) and A-type antiferromagnetic (A-AFM) structures on ABO_3 , drawn by VESTA⁴³. Here, the A-site ions are not shown. Blue and brown circles stand for the up and down spins on B-site, respectively. O1 and O2 sites are indicated by the red circles. In G-AFM, the neighbor magnetic moments are aligned antiparallel. In A-AFM, the magnetic moments are aligned parallel in a - b plane with antiparallel coupling with neighbor planes.

In a multiferroic system, an essential contribution of the quantum Berry phase of valence electrons can be revealed by the combined study of accurate structural analysis and first-principles calculation¹⁵. For tetragonal perovskite $Sr_{1/2}Ba_{1/2}MnO_3$, Giovannetti *et al.* performed the first-principles density functional theory (DFT) band simulation and claimed that the ferroelectric polarization caused by Mn-O2 hybridization is suppressed by Mn-O1-Mn superexchange interaction in the G-AFM ordering¹⁴. In their study, the crystal structure in the multiferroic phase was theoretically optimized with generalized gradient approximation (GGA) potential whereas the comparison with the experimental structure was missing. It is also noteworthy here that a simulation study can provide an ideal magnetic structure that enhances ferroelectricity. In the multiferroic materials, the change of the magnetic structure may induce much larger ferroelectric polarization^{16,17}. Thus, for the further understanding of the multiferroic properties in tetragonal perovskite $Sr_{1/2}Ba_{1/2}MnO_3$, it is important as well to evaluate the ferroelectric polarization in hypothetical magnetic structures.

In this paper, we report the atomic displacements in the ferroelectric and multiferroic phases of tetragonal perovskite $Sr_{1/2}Ba_{1/2}MnO_3$ determined by the crystal structure analyses using the twin-free single crystal and higher- Q diffraction data than earlier work⁸.

By the ferroelectric mode analyses, the polar crystal structures in the ferroelectric and multiferroic phases for $Sr_{1/2}Ba_{1/2}MnO_3$ and other tetragonal perovskite (ABO_3) were classified. By a first-principle calculation based on the accurate-crystal-structural parameters, we quantitatively clarify the suppression mechanism of the ferroelectric polarization in multiferroic phase and discuss the possible magnetic structure that enhances the electric polarization.

II. EXPERIMENTAL AND COMPUTATIONAL PROCEDURES

A single crystal of tetragonal perovskite $Sr_{1/2}Ba_{1/2}MnO_3$ was synthesized by a high-pressure treatment on the precursor sample of oxygen-deficient single crystals⁸. A synchrotron x-ray diffraction experiment was performed on BL02B1 at SPring-8, Japan¹⁸. The photon energy of the incident x rays was tuned at 35.04 keV. Using the high energy x-ray, we can access diffraction peaks with high spatial resolution up to $Q \sim 30 \text{ \AA}^{-1}$. The single crystal was crushed into cubes with a typical dimension of about $20 \mu\text{m}$. The absorption coefficient μ is calculated to be 37.85 cm^{-1} . The empirical absorption correction was carried out¹⁹. Rapid-Auto program (Rigaku Corp.) was used to obtain an F-table. CRYSTAL STRUCTURE (Rigaku Corp.) program was used for analyzing the crystal structure from the F-table. In the crystal structure analysis in the multiferroic phase at 50 K, the isotropic atomic displacement parameter B_{iso} was used for the Ba/Sr site.

First-principles calculations were performed using the VASP code²⁰ within the GGA + U ²¹ formalism with various U values. In addition, we employed the Heyd-Scuseria-Ernzerhof (HSE06) screened hybrid functional method²², which mixes the exact non-local Fock exchange and the density-functional parametrized exchange. The HSE06 is known to improve the evaluation of the band gap energy and the structural distortion, with respect to GGA + U approaches²³. The cut-off energy for the plane-wave expansion of the wavefunctions was set to 400 eV and a \mathbf{k} -point shell of (4, 4, 3) was used for the Brillouin zone integration according to Monkhorst-Pack special point mesh. The crystal structure was optimized with respect to internal atomic coordinates until the remaining forces were less than 1 meV/\AA while the lattice parameters were kept at the experimental values.

III. RESULTS AND DISCUSSION

A. Synchrotron x-ray diffraction and crystal structure analysis

The synchrotron x-ray diffraction experiments have been carried out in the ferroelectric ($T = 225 \text{ K}$) and

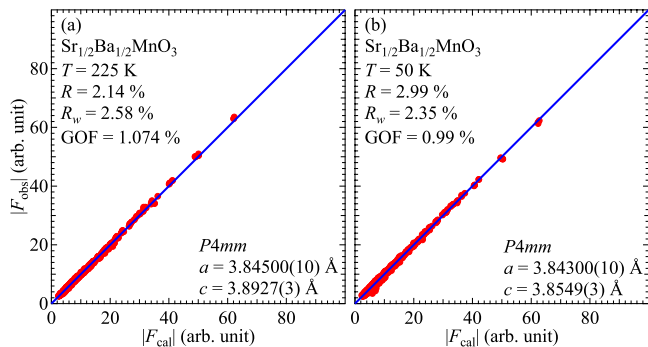


FIG. 2: (Color online) Comparison between observed ($|F_{\text{obs}}|$) and calculated ($|F_{\text{cal}}|$) structure factors (a) at 225 K in the ferroelectric and (b) at 50 K in the multiferroic phases of tetragonal perovskite $\text{Sr}_{1/2}\text{Ba}_{1/2}\text{MnO}_3$.

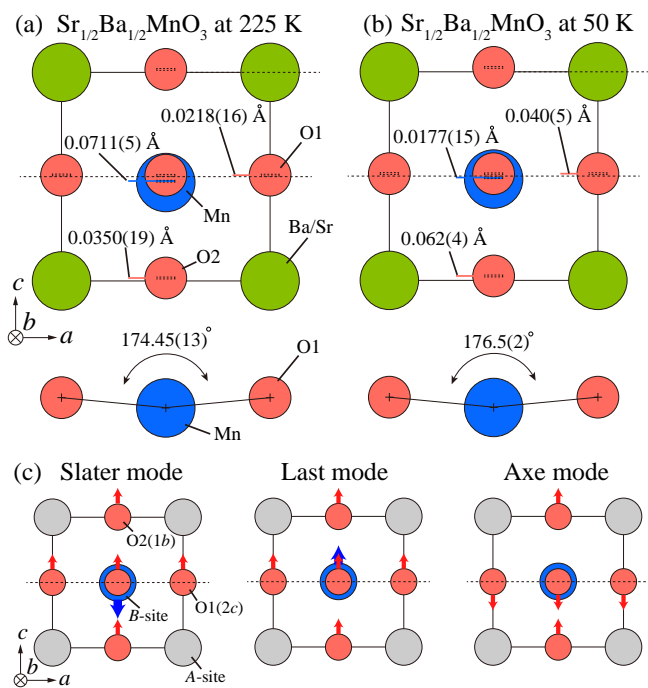


FIG. 3: (Color online) (a, b) The atomic displacements and O1-Mn-O1 bond angles of tetragonal perovskite $\text{Sr}_{1/2}\text{Ba}_{1/2}\text{MnO}_3$ at 225 K in the ferroelectric phase (a) and 50 K in the multiferroic phase (b). (c) Atomic displacements of the respective ferroelectric modes on the perovskite ABO_3 . Red and blue arrows stand for the directions of the displacement for the O and B-site ions, respectively.

in the multiferroic ($T = 50$ K) phases of tetragonal perovskite $\text{Sr}_{1/2}\text{Ba}_{1/2}\text{MnO}_3$. All observed diffraction spots can be indexed by those of the $P4mm$ space group. By using these data sets, we performed crystal structure analyses. Here, the A-site ion is fixed at the centrosymmetric position. The comparisons between observed and calculated structure factors are shown in Fig. 2. The structural parameters at 225 K and 50 K are summarized in Tables I and II, respectively. Schematic views of

the atomic displacements in the ferroelectric and multiferroic phases of tetragonal perovskite $\text{Sr}_{1/2}\text{Ba}_{1/2}\text{MnO}_3$ are shown in Figs. 3(a) and 3(b). As a reference, the O1-Mn-O1 bond angles of tetragonal BaTiO_3 and cubic SrMnO_3 are also shown in Fig. 1(a). In the ferroelectric phase of tetragonal perovskite $\text{Sr}_{1/2}\text{Ba}_{1/2}\text{MnO}_3$, the atomic displacements along the c -axis at 225 K are respectively 0.0711(5) Å for Mn ion, 0.0218(16) Å for O1 (2c site), and 0.0350(19) Å for O2 (1b site), which are of the same order of magnitude as those reported by the earlier study⁸. The off-centering distortion can be estimated by the O1-Mn-O1 bond angle, as 174.45(13)° at 225 K in the ferroelectric phase, comparable with that of tetragonal BaTiO_3 ²⁴.

The atomic displacements and O1-Mn-O1 distortion at 50 K in the multiferroic phase are respectively changed as 0.0177(15) Å for Mn ion, 0.040(5) Å for O1, 0.062(4) Å for O2, and 176.5(2)°. In this study, since the atomic displacements are determined with the accuracy of the 10^{-3} Å order, we observed that the atomic displacements of O ions are larger than that of Mn ion in the multiferroic phase. This enlarged atomic displacements of the O ions can not be explained only by the suppression of the off-centering distortion. The reason for this enlargement will be discussed later.

Next, we analyzed the observed atomic displacements by the ferroelectric modes to compare the ferroelectric and multiferroic phases of tetragonal perovskite $\text{Sr}_{1/2}\text{Ba}_{1/2}\text{MnO}_3$ with other ferroelectric perovskite materials. At the structural phase transition from cubic $Pm\bar{3}m$ to tetragonal $P4mm$ in the perovskite oxide, the polar vibrational motion is decomposed by three modes, so-called Slater, Last, and Axe modes [See Fig. 3(c)]. The analysis by these ferroelectric modes is commonly performed to classify the soft phonon mode obtained from the optical, x-ray, and neutron spectroscopy experiments^{25–30}. In this paper, we used polar atomic displacements from centrosymmetric positions to estimate frozen ferroelectric modes. The ratio of the frozen ferroelectric modes in tetragonal perovskite $\text{Sr}_{1/2}\text{Ba}_{1/2}\text{MnO}_3$ are compared with those in other ferroelectrics in Table III. The frozen ferroelectric modes can be quantified from the masses and the atomic displacements from the centrosymmetric positions of ions, as Harada *et al.* did using the inelastic structure factor of the soft phonon modes³¹. Here, the polar atomic displacements of B-site, O1, and O2 sites are represented by ξ_B , ξ_{O1} , and ξ_{O2} , respectively. The coefficients of the ferroelectric modes, S_{Slater} , S_{Last} , and S_{Axe} , can be defined as

$$\xi_x = S_{\text{Slater}} \cdot \mathbf{s}_{\text{Slater}} + S_{\text{Last}} \cdot \mathbf{s}_{\text{Last}} + S_{\text{Axe}} \cdot \mathbf{s}_{\text{Axe}}. \quad (1)$$

$$\xi_x = (\xi_B, \xi_{O1}, \xi_{O2}).$$

Here, $\mathbf{s}_{\text{Slater}} = (-k, 1, 1)$, $\mathbf{s}_{\text{Last}} = (1 + k', 1 + k', 1 + k')$, $\mathbf{s}_{\text{Axe}} = (0, -1/2, 1)$, $k = 3M_O/M_B$, and $k' = (M_B + 3M_O)/M_A$. M_A , M_B , and M_O stand for the mass of

TABLE I: Structure parameters of $\text{Sr}_{1/2}\text{Ba}_{1/2}\text{MnO}_3$ at 225 K in the ferroelectric phase (Space group $P4mm$ (No. 99)). The 22953 reflections were observed, and 3455 of them are independent. The 17 variables were used for the refinement. The lattice parameters are $a = 3.84500(10)$ Å and $c = 3.8927(3)$ Å. The reliability factors are $R = 2.14\%$, $R_w = 2.58\%$, GOF(Goodness of fit) = 1.074. In the tables, x , y , and z are the fractional coordinates. Anisotropic atomic displacement parameters are represented as U_{11} , U_{22} , U_{33} , U_{12} , U_{13} , and U_{23} .

	site	x	y	z	B_{eq}	occupancy
Ba/Sr	1a	0	0	0	0.36(5)	1/2
Mn	1b	1/2	1/2	0.48173(13)	0.3032(15)	1
O1	2c	0	1/2	0.5056(4)	0.609(7)	1
O2	1b	1/2	1/2	0.0090(5)	0.658(8)	1

	U_{11} (Å ²)	U_{22} (Å ²)	U_{33} (Å ²)	U_{12} (Å ²)	U_{13} (Å ²)	U_{23} (Å ²)
Ba	0.00529(7)	0.00529(7)	0.00313(11)	0	0	0
Sr	0.00409(9)	0.00409(9)	0.00009(8)	0	0	0
Mn	0.00450(3)	0.00450(3)	0.00252(6)	0	0	0
O1	0.00465(13)	0.00908(19)	0.0094(2)	0	0	0
O2	0.00935(19)	0.00935(19)	0.0063(2)	0	0	0

TABLE II: Structure parameters of $\text{Sr}_{1/2}\text{Ba}_{1/2}\text{MnO}_3$ at 50 K in the multiferroic phase (Space group $P4mm$ (No. 99)). The 23321 reflections were observed, and 3409 of them are independent. The 14 variables were used for the refinement. The lattice parameters are $a = 3.84300(10)$ Å and $c = 3.8549(3)$ Å. The reliability factors are $R = 2.99\%$, $R_w = 2.35\%$, GOF(Goodness of fit) = 0.99. In Ba/Sr site, the isotropic atomic displacement parameter is used for the crystal structure analysis.

	site	x	y	z	$B_{\text{iso}}/B_{\text{eq}}$	occupancy
Ba/Sr	1a	0	0	0	0.31(5)	1/2
Mn	1b	1/2	1/2	0.4954(4)	0.298(2)	1
O1	2c	0	1/2	0.5105(13)	0.500(8)	1
O2	1b	1/2	1/2	0.0161(11)	0.472(12)	1

	U_{11} (Å ²)	U_{22} (Å ²)	U_{33} (Å ²)	U_{12} (Å ²)	U_{13} (Å ²)	U_{23} (Å ²)
Mn	0.00355(3)	0.00355(3)	0.00424(15)	0	0	0
O1	0.00414(16)	0.0068(2)	0.0080(3)	0	0	0
O2	0.00680(19)	0.00680(19)	0.0043(5)	0	0	0

A-site, B-site, and O ions, respectively. Thus,

$$\begin{pmatrix} \xi_B \\ \xi_{\text{O1}} \\ \xi_{\text{O2}} \end{pmatrix} = \begin{pmatrix} -k & 1+k' & 0 \\ 1 & 1+k' & -\frac{1}{2} \\ 1 & 1+k' & 1 \end{pmatrix} \begin{pmatrix} S_{\text{Slater}} \\ S_{\text{Last}} \\ S_{\text{Axe}} \end{pmatrix}, \quad (2)$$

$$\begin{pmatrix} S_{\text{Slater}} \\ S_{\text{Last}} \\ S_{\text{Axe}} \end{pmatrix} = \alpha \begin{pmatrix} \xi_B \\ \xi_{\text{O1}} \\ \xi_{\text{O2}} \end{pmatrix}, \text{ and} \quad (3)$$

$$\alpha = \frac{1}{3(1+k)} \begin{pmatrix} -3 & 2 & 1 \\ \frac{3}{1+k'} & \frac{2k}{1+k'} & \frac{k}{1+k'} \\ 0 & -2(1+k) & 2(1+k) \end{pmatrix}.$$

In Table III, the coefficients of the ferroelectric modes are summarized for tetragonal perovskite $\text{Sr}_{1/2}\text{Ba}_{1/2}\text{MnO}_3$, in comparison for other perovskite ferroelectrics, tetragonal BaTiO_3 , KNbO_3 , PbTiO_3 , and BiCoO_3 ^{9,24,32,33}.

In the ferroelectric phase of tetragonal perovskite $\text{Sr}_{1/2}\text{Ba}_{1/2}\text{MnO}_3$, the dominant positive S_{Slater} , relatively large negative S_{Last} , and small positive S_{Axe} are obtained. The contributions from the $|S_{\text{Slater}}|$, $|S_{\text{Last}}|$,

and $|S_{\text{Axe}}|$ are approximately 70 %, 18 %, and 12 %, compatible with the result (71 %, 24 %, and 5 %) obtained by the optical and inelastic x-ray spectroscopies³⁰. In tetragonal BaTiO_3 , the dominant positive S_{Slater} , small negative S_{Last} , and relatively large positive S_{Axe} are observed. In tetragonal KNbO_3 , the positive S_{Slater} is dominant but the error bars for the other modes are too large. As a commonality, they share two characteristics, the dominant positive S_{Slater} and negative S_{Last} .

To explain the origin of the commonality, we refer the earlier first-principles calculations for perovskite oxides, which have pointed out the importance of the covalency between the B-site and the apical O2 ions for the emergence of ferroelectricity³⁴⁻³⁷. This is the reason why the dominant parameter is the Slater mode with contracting the distance between the B-site and O2 ions as shown in Fig. 3(c). The negative S_{Last} and positive S_{Axe} play a role in reducing the extra atomic displacements of the O1 ions generated by the Slater mode.

In PbTiO_3 , the earlier first-principles calculation also pointed out that the hybridization between the 6p band of Pb and 2p band of O1 induces additional component of the electric polarization³⁶. In that case, the distance be-

TABLE III: Frozen ferroelectric modes estimated from the atomic displacements for B -site and O ions in the tetragonal ferroelectric and multiferroic phases. S_{Slater} , S_{Last} , and S_{Axe} stand for the coefficients of Slater, Last, and Axe ferroelectric modes, respectively. The contribution ratio from the $|S_{\text{Slater}}|$, $|S_{\text{Last}}|$, and $|S_{\text{Axe}}|$ are also shown in brackets. ξ_B , ξ_{O1} , ξ_{O2} are respectively the atomic displacements for B , O1, and O2 sites. Here, we selected the sign of the atomic displacement ξ_B so that the S_{Slater} is positive. \angle_{O1BO1} stands for the distortion of O1- B -O1 bond angle.

	ξ_B (Å)	ξ_{O1} (Å)	ξ_{O2} (Å)	S_{Slater}	S_{Last}	S_{Axe}	\angle_{O1BO1} (deg)
$\text{Sr}_{1/2}\text{Ba}_{1/2}\text{MnO}_3$ (225 K)	-0.0711(5)	0.0218(16)	0.0350(19)	0.0519(13) [70 %]	-0.0134(9) [18 %]	0.009(2) [12 %]	174.45(13)
$\text{Sr}_{1/2}\text{Ba}_{1/2}\text{MnO}_3$ (50 K)	-0.0177(15)	0.040(5)	0.062(4)	0.035(4) [63 %]	0.007(2) [13 %]	0.014(5) [25 %]	176.5(2)
BaTiO_3 [24] (300 K)	-0.091(2)	0.042(2)	0.0985(16)	0.076(2) [62 %]	-0.0087(17) [7 %]	0.037(2) [30 %]	172.4(2)
KNbO_3 [9] (543 K)	-0.09(4)	0.08(4)	0.07(4)	0.11(5) [86 %]	-0.008(19) [6 %]	-0.01(5) [8 %]	170.2(3)
PbTiO_3 [32] (295 K)	0.1567(16)	0.4879(13)	0.4646(13)	0.1615(15) [41 %]	0.2178(12) [55 %]	-0.0155(15) [4 %]	160.7(2)
BiCoO_3 [33] (300 K)	0.316(4)	1.086(2)	0.961(2)	0.402(4) [44 %]	0.425(3) [47 %]	-0.084(3) [9 %]	135.1(2)

tween the Pb and O1 ions also decreases. This atomic displacement induces the combined S_{Slater} and S_{Last} mode, which can be actually seen in PbTiO_3 , as listed in Table III. In BiCoO_3 , since the ratio of the ferroelectric modes is similar with that of PbTiO_3 , we speculate that the origin of the ferroelectricity for BiCoO_3 is the same for PbTiO_3 .

In the multiferroic phase of $\text{Sr}_{1/2}\text{Ba}_{1/2}\text{MnO}_3$, S_{Slater} and S_{Last} are suppressed, while S_{Axe} is enlarged. In addition, the sign of S_{Last} changes to positive. The G-AFM exchange interaction prefers 180° O1-Mn-O1 bond angle, being contradictory with off-centering distortion of O1-Mn-O1 bond angle. Therefore, the displacement for Mn ion is suppressed, and consequently gives rise to the decrease of S_{Slater} and S_{Last} modes. In stark contrast, the apical O2 is relatively free from the restriction of the magnetic exchange interaction. Thus, we speculate that the atomic displacement for apical O2 is enlarged to obtain the gain of the covalency between Mn and O2, resulting in the enlarged S_{Axe} parameter. To eliminate the extra atomic displacements of the O1 from S_{Axe} , the sign of S_{Last} mode changes to positive in the multiferroic phase. From the experimentally determined crystal structure information and the results of the mode analyses, we discussed and speculated the qualitative suppression mechanism of the ferroelectricity. To support this speculation and provide more quantitative discussion, we performed the first-principles calculation.

B. First-principles calculation

For the discussion of the atomic displacements and the resulting ferroelectricity in this system, we performed first-principles calculations for tetragonal perovskite $\text{Sr}_{1/2}\text{Ba}_{1/2}\text{MnO}_3$. To understand the effect of the magnetic order upon the ferroelectricity in the multiferroic phase, here we also simulate the ferroelectric polar-

ization in the hypothetical A-type antiferromagnetic (A-AFM) structure (the magnetic moments are aligned parallel in a - b plane with antiparallel coupling with neighbor planes as shown in Fig. 1(b)) as well as the ground-state G-AFM structure in $\text{Sr}_{1/2}\text{Ba}_{1/2}\text{MnO}_3$.

Figures 4(a) and 4(b) show the density of states from GGA + U calculations. When we set $U = 3$ eV and $J = 1$ eV as consistent with the previous DFT study¹⁴, the system is insulator while the energy gap is significantly underestimated as $E_{\text{gap}} \sim 0.5$ eV, being inconsistent with the experimentally estimated energy gap ~ 2 eV for SrMnO_3 ³⁸. The underestimation of the energy gap was not improved when the U value was increased up to 6 eV [see Fig. 4(b)]; on the contrary, the band gap was reduced to be ~ 0.3 eV. This result might seem counterintuitive but this is due to a property of GGA + U method that adds effective Coulomb potential only to the localized orbital states (such as $3d$ and $4f$ orbital states). Indeed, GGA + U Coulomb potential shifts down the occupied Mn $3d$ states but keeps delocalized O $2p$ states at the original energy levels around the valence top state. When the O $2p$ states are located at shallow energy level, Mn ion favors to show trivalent instead of quadrivalent ionic state. This is the reason why the band gap tends to be closed as increasing the U value. To make matters worse, this narrow energy gap is closed when hypothetical ferromagnetic phase or A-AFM phase is calculated. Therefore, we conclude that GGA + U approach is not appropriate to describe the wide gapped insulating state and evaluate the ferroelectric distortion in $\text{Sr}_{1/2}\text{Ba}_{1/2}\text{MnO}_3$.

Figure 4(c) shows the density of states from HSE06 calculation, leading to the wider energy gap ($E_{\text{gap}} \sim 2$ eV, consistent with the experimental data in SrMnO_3 ³⁸) with Mn quadrivalent state. In this case, the fraction of exact Hartree-Fock exchange in HSE06 scheme shifts down both the occupied Mn $3d$ levels and O $2p$ levels. Hereinafter, we will focus on HSE06 results and discuss the

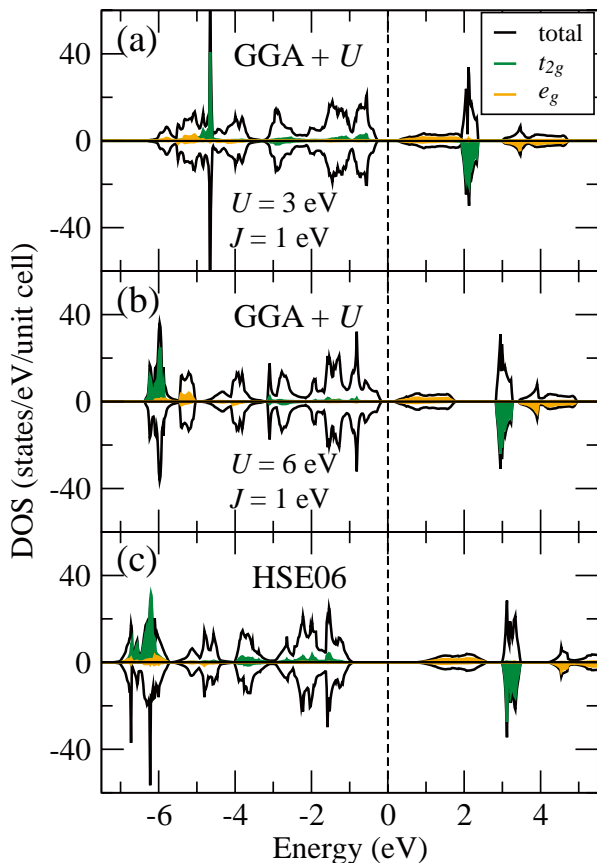


FIG. 4: Density of states (DOS) in G-AFM of $\text{Sr}_{1/2}\text{Ba}_{1/2}\text{MnO}_3$ calculated from GGA + U method with (a) $U = 3$ eV and $J = 1$ eV, (b) $U = 6$ eV and $J = 1$ eV, and from (c) HSE06 method. Upper and lower panels show majority- and minority-spin states, respectively. Projected DOS for Mn t_{2g} and e_g orbital states are highlighted with green and orange colors, respectively.

ferroelectric property. By using the experimental and DFT-optimized crystal structures, the ferroelectric polarization was calculated as listed in Table IV. In order to investigate the influence of the magnetic ordering to the ferroelectric polarization, we consider the ground-state G-AFM and the hypothetical A-AFM configurations.

It is noted that the calculated electric polarization by the optimized structure based on point-charge model with nominal ionic charges (Ba and Sr; 2+, Mn; 4+, O; 2-), *i.e.*, the ionic displacement contribution to the electric polarization, shows good agreement with that estimated by the experimental crystal structure: $P_{\text{PCM}} \sim 10.1 \mu\text{C}/\text{cm}^2$ with G-AFM in both experimental and optimized structures at $T = 50$ K. This result supports the advantage of use of HSE06 functional for the polar structural distortion with a high accuracy. The total electric polarization P_{Berry} , *i.e.*, the summation of ionic and electronic contributions, is almost double of the P_{PCM} , as often seen in other ferroelectric manganites³⁹, and is of the same order of magnitude with the electric polariza-

TABLE IV: Calculated ferroelectric polarization for the experimental (E) and optimized (O) crystal structure at $T = 50$ K for the G-AFM and A-AFM antiferromagnetic ordering as based on HSE06-exchange-correlation functional. Both the net polarization obtained by Berry phase method (P_{Berry}) and the ionic contribution based on point charge model (P_{PCM}) are shown in unit of $\mu\text{C}/\text{cm}^2$.

	$E_{\text{G-AFM}}$	$E_{\text{A-AFM}}$	$O_{\text{G-AFM}}$	$O_{\text{A-AFM}}$
P_{Berry}	19.37	23.65	20.17	30.24
P_{PCM}	10.05	10.05	10.11	15.45

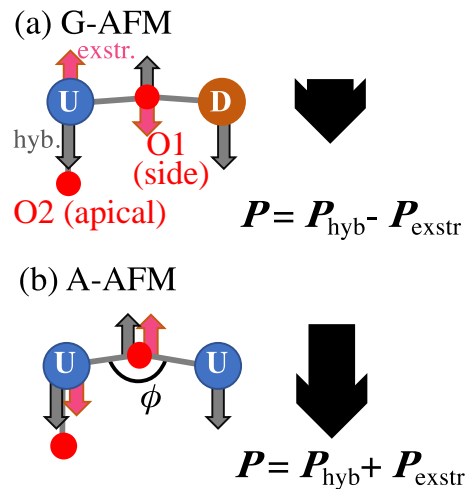


FIG. 5: Schematic illustration of ionic distortion (narrow gray and red arrows) and induced electric polarization P (wide black arrows) for (a) G-type (G-AFM) and (b) A-type (A-AFM) antiferromagnetic orderings. Narrow gray and red arrow stand for the atomic displacement originating from the hybridization between Mn 3d and apical O2 2p bands and the in-plane Mn-O1-Mn magnetic magnetic exchange striction, respectively. P_{hyb} and P_{exstr} stand for the electric polarization from the hybridization and the exchange striction, respectively. U and D denote up- and down-spins Mn sites, respectively. The detailed crystal and magnetic structures are shown in Fig. 1(b).

tion ($13.5 \mu\text{C}/\text{cm}^2$) experimentally obtained in the earlier study⁸.

Next, we focus on the the suppression mechanism of the ferroelectricity in the multiferroic phase. Basically, we consider two mechanisms to induce the polarization: hybridization between Mn 3d and apical O2 2p states (P_{hyb}), and in-plane Mn-O1-Mn magnetic exchange striction (P_{exstr}) as shown in Fig. 5. The $p-d$ hybridization drives polar ionic distortion of Slater mode, by which Mn and O2 ions are respectively shifted downward and upward. The magnetic exchange striction modulates the in-plane Mn-O1-Mn bond angle (ϕ), resulting in the suppression of the S_{Slater} and the sign change of S_{Last} . Since the driving mechanism of the change of the ferroelectricity upon the ferroelectric to multiferroic phase transition is the magnetic exchange interaction, the atomic

displacement should depend on the Mn spin configuration. In G-AFM, the magnetic exchange striction favors $\phi = 180^\circ$ so that Goodenough-Kanamori rule is satisfied for Mn^{4+} ion^{40–42}. This magnetic exchange striction prevents the atomic displacement of the side O1 ion so that total electric polarization is reduced. In contrast, in case of the hypothetical A-AFM, the magnetic exchange striction favors $\phi = 90^\circ$ and enhances the hybridization-induced polarization as shown in Fig. 5. The calculated polarization with G-AFM and A-AFM is $P_{\text{Berry}} = 20.17$ and $30.24 \mu\text{C}/\text{cm}^2$, respectively, as being consistent with the above discussed mechanism. The difference of the P values allows us to decompose the polarization into two contributions, $P_{\text{hyb}} \sim 25$ and $P_{\text{extr}} \sim 5 \mu\text{C}/\text{cm}^2$. The former is comparable to the conventional ferroelectric polarization in BaTiO_3 ($P \sim 26 \mu\text{C}/\text{cm}^2$) and the latter is comparable to the magnetically-driven polarization in multiferroic HoMnO_3 ($P \sim 6 \mu\text{C}/\text{cm}^2$)³⁹. Thus, we conclude that since only positive P_{hyb} contributes the ferroelectric polarization in the paramagnetic phase, negative P_{extr} causes the suppression of the polarization observed in the multiferroic phase. If one succeeded in stabilizing A-AFM in tetragonal AMnO_3 system, it might be a milestone multiferroic demonstrating the polarization larger than representative ferroelectric BaTiO_3 . Nonetheless, since A-AFM is energetically unfavored by 1.2 eV/f.u. with respect to G-AFM, a study to stabilize the A-AFM AMnO_3 is left as a topic for future work.

IV. SUMMARY

In summary, we have performed the synchrotron x-ray diffraction experiment to investigate the accurate crystal structures in the ferroelectric and multiferroic phases of tetragonal perovskite $\text{Sr}_{1/2}\text{Ba}_{1/2}\text{MnO}_3$ using twin-free-single-crystalline sample. The large atomic displacement

for Mn ion was observed in the ferroelectric phase. In the multiferroic phase, by contrast the atomic displacement for Mn ion is suppressed, but those for O ions are enlarged. From the obtained crystal structural parameters, the ferroelectric mode analyses were carried out. In the ferroelectric phase, the atomic displacements can be decomposed as dominant positive Slater, negative Last, and small positive Axe modes. The suppression of Slater and Last modes, the sign change of Last mode, and the enlargement of Axe mode are found in the multiferroic phase. The first-principles calculation using HSE06 functional successfully described the wide-gap insulating electronic states and quantitatively reproduces the experimentally observed ferroelectric polarization. The calculated ferroelectric polarization is further decomposed into two parts relevant to the hybridization and exchange striction mechanisms.

Acknowledgments

The authors are grateful to T. Arima and H. Katsumoto for fruitful discussions. The synchrotron x-ray diffraction experiment was performed at SPring-8 with approval of the JASRI (Proposal Numbers 2009B1304 and 2010A1795). This work was in part supported by Grant-in-Aids for Scientific Research (Nos. 17H02916, 17K14327, 19K03709, and 19H05822) from the Ministry of Education, Culture, Sports, Science and Technology (MEXT), Japan, and by the Research Program for CORE lab of "Dynamic Alliance for Open Innovation Bridging Human, Environment and Materials" in "Network Joint Research Center for Materials and Devices". The computation in this work has been partially done using the facilities of the Supercomputer Center, the Institute for Solid State Physics, the University of Tokyo.

* okudaisu@tohoku.ac.jp

¹ T. Kimura, T. Goto, H. Shintani, K. Ishizaka, T. Arima, and Y. Tokura, *Nature (London)* **426**, 55 (2003).

² M. Fiebig *J. Phys. D:Appl.Phys.* **38** R123 (2005).

³ S. W. Cheong, and M. Mostovoy *Nature Mater.* **6** 13 (2007).

⁴ Y. Tokura, S. Seki and N. Nagaosa, *Rep. Prog. Phys.* **77** 076501 (2014).

⁵ S. Bhattacharjee, E. Bousquet, and P. Ghosez, *Phys. Rev. Lett.* **102**, 117602 (2009).

⁶ J. M. Rondinelli, A. S. Eidelson, and N. A. Spaldin, *Phys. Rev. B* **79**, 205119 (2009).

⁷ J. H. Lee and K. M. Rabe, *Phys. Rev. Lett.* **104**, 207204 (2010).

⁸ H. Sakai, J. Fujioka, T. Fukuda, D. Okuyama, D. Hashizume, F. Kagawa, H. Nakao, Y. Murakami, T. Arima, A. Q. R. Baron, Y. Taguchi, and Y. Tokura, *Phys. Rev. Lett.* **107**, 137601 (2011).

⁹ A. W. Hewat, *J. Phys. C : Solid State Phys.*, **6**, 2559

(1973).

¹⁰ B. C. Frazer, H. R. Danner, and R. Pepinsky, *Phys. Rev.* **100**, 745 (1955).

¹¹ G. Shirane H. Danner, and R. Pepinsky, *Phys. Rev.* **105**, 856 (1957).

¹² T. Takeda, and S. Ōhara, *J. Phys. Soc. Jpn.* **37**, 275 (1974).

¹³ O. Chmaissem, B. Dabrowski, S. Kolesnik, J. Mais, D. E. Brown, R. Kruk, P. Prior, B. Pyles, and J. D. Jorgensen, *Phys. Rev. B* **64**, 134412 (2001).

¹⁴ G. Giovannetti, S. Kumar, C. Ortix, M. Capone and J. van den Brink, *Phys. Rev. Lett.* **109**, 107601 (2012).

¹⁵ D. Okuyama, S. Ishiwata, Y. Takahashi, K. Yamauchi, S. Picozzi, K. Sugimoto, H. Sakai, M. Takata, R. Shimano, Y. Taguchi, T. Arima, and Y. Tokura, *Phys. Rev. B* **84**, 054440 (2011).

¹⁶ O. Prokhnenko, R. Feyerherm, E. Dudzik, S. Landsgesell, N. Aliouane, L. C. Chapon, and D. N. Argyriou, *Phys. Rev. Lett.* **98**, 057206 (2007).

¹⁷ S. Ishiwata, Y. Kaneko, Y. Tokunaga, Y. Taguchi, T.-

- h. Arima, and Y. Tokura, *Phys. Rev.* **B 81**, 100411(R) (2010).
- ¹⁸ K. Sugimoto, H. Ohsumi, S. Aoyagi, E. Nishibori, C. Moriyoshi, Y. Kuroiwa, H. Sawa, and M. Takata, *AIP Conf. Proc.* **1234** 887 (2010).
- ¹⁹ T. Higashi, *Abscor -Empirical Absorption Correction based on Fourier Series Approximation*. Rigaku Corporation, Tokyo, Japan (1995).
- ²⁰ G. Kresse, and J. Furthmüller, *Phys. Rev.* **B 54**, 11169 (1996).
- ²¹ V. I. Anisimov, F. Aryasetiawan, and A. I. Lichtenstein, *J. Phys.: Condens. Matter.* **9**, 767 (1997).
- ²² J. Heyd, G. E. Scuseria, and M. Ernzerhof, *J. Chem. Phys.* **118**, 8207 (2003).
- ²³ A. Stroppa and S. Picozzi, *Phys. Chem. Chem. Phys.* **12**, 5405 (2010).
- ²⁴ G. H. Kwei, A. C. Lawson, S. J. L. Billinge, and S.-W. Cheong, *J. Phys. Chem.* **97**, 2368 (1993).
- ²⁵ W. Cochran, *Adv. Phys.* **9**, 387 (1960).
- ²⁶ G. Shirane, J. D. Axe, J. Harada, and J. P. Remeika, *Phys. Rev.* **B 2**, 155 (1970).
- ²⁷ A. C. Nunes, J. D. Axe and G. Shirane, *Ferroelectrics* **2**, 291 (1971).
- ²⁸ J. Harada, J. D. Axe and G. Shirane, 1971, *Phys. Rev.* **B 4**, 155 (1971).
- ²⁹ J. F. Scott, *Rev. Mod. Phys.* **46**, 83 (1974).
- ³⁰ H. Sakai, J. Fujioka, T. Fukuda, M. S. Bahramy, D. Okuyama, R. Arita, T. Arima, A. Q. R. Baron, Y. Taguchi, and Y. Tokura, *Phys. Rev.* **B 86**, 104407 (2012).
- ³¹ J. Harada, J. D. Axe, and G. Shirane, *Acta Cryst.* **A26**, 608 (1970).
- ³² R. J. Nelmes and W. F. Kuhs, *Solid State Commun.* **54**, 721 (1985).
- ³³ A. A. Belik, S. Iikubo, K. Kodama, N. Igawa, S. Shamoto, S. Niitaka, M. Azuma, Y. Shimakawa, M. Takano, F. Izumi, and E. Takayama-Muromachi, *Chem. Mater.* **18**, 798 (2006).
- ³⁴ R. E. Cohen, *Nature* **358** 136 (1992).
- ³⁵ R. E. Cohen and H. Krakauer, *Ferroelectrics* **136** 65 (1992).
- ³⁶ H. Miyazawa, E. Natori, S. Miyashita, T. Shimoda, F. Ishii, and T. Oguchi, *Jpn. J. Appl. Phys.* **39**, 5679 (2000).
- ³⁷ A. Chassé, St. Borek, K.-M. Schindler, M. Trautmann, M. Huth, F. Steudel, L. Makhova, J. Gräfe, and R. Denecke, *Phys. Rev.* **B 84**, 195135 (2011).
- ³⁸ T. Saitoh, A. E. Bocquet, T. Mizokawa, H. Namatame, A. Fujimori, M. Abbate, Y. Takeda, and M. Takano, *Phys. Rev.* **B 51**, 13942 (1995).
- ³⁹ S. Picozzi, K. Yamauchi, B. Sanyal, I. A. Sergienko, and E. Dagotto, *Phys. Rev. Lett.* **99**, 227201 (2007).
- ⁴⁰ J. B. Goodenough, *Phys. Rev.* **100**, 564 (1955).
- ⁴¹ J. B. Goodenough, *J. Phys. Chem. Solids* **6**, 287 (1958).
- ⁴² J. Kanamori, *J. Phys. Chem. Solids* **10**, 87 (1959).
- ⁴³ K. Momma and F. Izumi, *J. Appl. Crystallogr.* **44**, 1272 (2011).